Applied Materials Today 29 (2022) 101630

Contents lists available at ScienceDirect

Applied Materials Today

journal homepage: www.elsevier.com/locate/apmt

Superhydrophobic surface processing for metal 3D printed parts

Wuji Huang [a], Benjamin Nelson [a,b], Steven Tian [c], Ramin Ordikhani-Seyedlar [d], Raymond C.Y. Auyeung [e], Avik Samanta [f], Hui Hu [g], Scott Shaw [d], Caterina Lamuta [a], Hongtao Ding [a,*]

[a] Department of Mechanical Engineering, University of Iowa, Iowa City, IA 52242, United States of America
[b] Quad City Manufacturing Laboratory, Western Illinois University, Rock Island, IL 61201, United States of America
[c] Department of Mechanical Engineering, Columbia University, New York, NY 10027, United States of America
[d] Department of Chemistry, University of Iowa, Iowa City, IA 52242, United States of America
[e] Naval Research Laboratory, Washington, DC 20375, United States of America
[f] Pacific Northwest National Laboratory, Richland, WA 99354, United States of America
[g] Department of Aerospace Engineering, Iowa State University, Ames, IA 50011, United States of America

ARTICLE INFO

Keywords:
Superhydrophobic Surface
Metal 3D Printing
Laser Powder Bed Fusion
Surface Functionalization

ABSTRACT

Surface engineering methods for wettability modification of 3D-printed metal parts have attracted considerable attention, in large part due to the applicability of these components in fluid-related fields. In this study, two processing methods have been developed to produce superhydrophobic surfaces on AlSi10Mg and Ti6Al4V fabricated using laser powder bed fusion (L-PBF). Surface chemistry and topography are investigated as two primary determinants of the resulting wettability state. On its own, chemical immersion treatment can impart the rose petal effect on these additively manufactured metal surfaces, viz. high water contact angle coupled with high water adhesion. When laser surface texturing is performed prior to chemical treatment, the lotus leaf effect is achieved instead, with the surface showing high water contact angles and low water adhesion. Surface chemistry analysis shows that a fluorosilane reagent reacts more favorably with laser textured surfaces, thus imparting greater hydrophobicity. Surface topography is also shown to play a significant role in the resulting wetting behavior. By applying surface topography parameters, S_{pc} and r, the topographical distinction between surfaces displaying the rose petal effect and the lotus leaf effect is quantitatively described.

1. Introduction

Surface wettability engineering for metal additive manufacturing (AM), or 3D printing, is of great significance. Many of these AM parts are used in applications involving fluid-surface interactions and fluid flow, such as marine parts, heat exchangers, battery devices, and bio-microfluidic devices [1–3]. Among many techniques for metal printing, selective laser melting (SLM), also defined by the ISO/ASTM as laser powder bed fusion (L-PBF), is widely applied for fabricating high-performance metal parts. The metal surfaces produced by L-PBF are generally rough due to the uneven distribution of laser radiation during fabrication and are generally hydrophilic, as metal alloys inherently have a high level of surface energy. However, the wetting behavior of printed parts is typically unstable and is subject to change after fabrication and cleaning. For instance, an increase in water contact angle from less than 10° to over 150° was reported for 3D printed 316L stainless steels after exposure to air for two weeks [4]. This wetting instability is a serious issue plaguing these AM metal parts, preventing them from meeting the performance standards demanded by fluid applications. Only a few previous reports [4,5] have studied the instability of surface wetting behaviors of laser additively manufactured components. This study attempts to first evaluate the surface wettability of L-PBFed parts, and then to develop a surface processing method to achieve stable superhydrophobicity by engineering the surface topography and chemistry.

For ease of reference, we define surface wettability as the following. The surface is defined as superhydrophobic when the water contact angle θ_w is higher than 150°, moderately hydrophobic when θ_w is from 120° to 150°, and slightly hydrophobic for θ_w values ranging from 90° to 120°. Similarly, superhydrophilic surfaces have a θ_w value smaller than 10°, moderately hydrophilic surfaces have θ_w values from 10° to 60°, and slightly hydrophilic surfaces have θ_w values from 60° to 90°.

* Corresponding author.
E-mail address: hongtao-ding@uiowa.edu (H. Ding).

https://doi.org/10.1016/j.apmt.2022.101630
Received 26 May 2022; Received in revised form 9 August 2022; Accepted 20 August 2022
Available online 29 August 2022

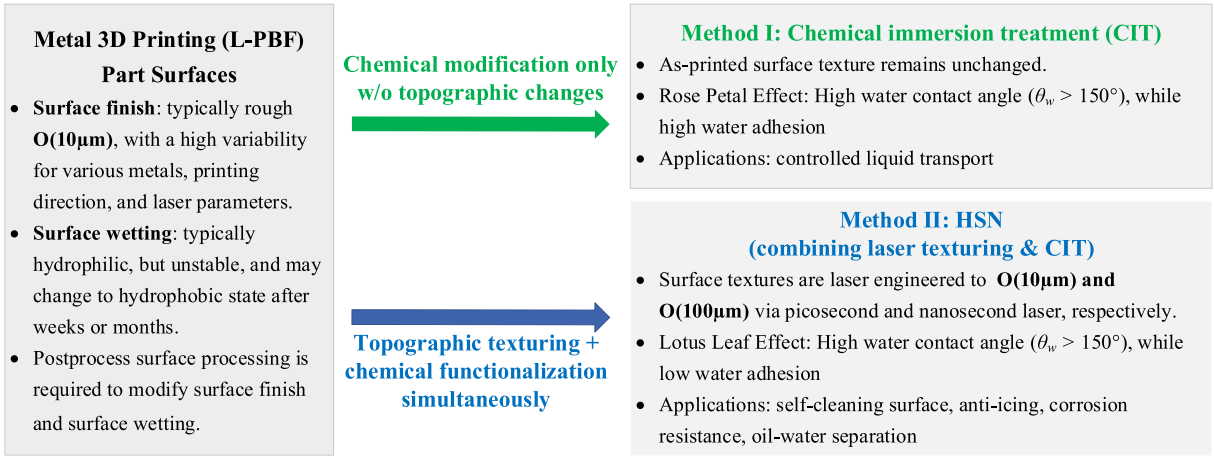

Fig. 1. Proposed superhydrophobic surface processing methods for metal 3d printed parts.

For stainless steel, Sun et al. [4] showed that as-printed 316L stainless steel without any specially designed surface structure is slightly hydrophobic (θ_w~96°), while a surface with an inverted trapezoidal structure is superhydrophilic (θ_w<10°). Neukaufer et al. [6] reported that a range of contact angle values from 70° to 92° can be achieved for raw 316L stainless steel by varying the printing orientation. Additionally, θ_w values of 80-100° were found on an L-PBFed 316L stainless steel surface with square pillars and rectangular channels [7]. For aluminum alloy, a slightly hydrophilic surface (θ_w~70°) was reported for AlSi10Mg parts made by L-PBF [8]. For titanium alloy, it has been found that an as-built L-PBFed Ti6Al4V surface is slightly hydrophilic (θ_w~70°) [9], while another group [10] reported the wettability of L-PBFed TA6V titanium alloy ranging from slight hydrophilicity (θ_w~75°) to slight hydrophobicity (θ_w~105°). Vaithilingam et al. [11] reported that a polished L-PBFed Ti6Al4V surface is moderately hydrophilic (θ_w~24°). Potential factors responsible for the discrepancy among these studies include variations in laser operating parameters, post-processing and cleaning methods, and the storage time in air after fabrication [12,13].

Various surface modification methods have been applied to achieve desirable wettability behavior on L-PBFed parts [14–16], most of which are used to create low-adhesion lotus leaf superhydrophobic surfaces. A popular technique involves treating surfaces bearing a specific surface morphology using chemical reagents. Sun et al. [4] created inverted trapezoidal structures on 316L stainless steel by L-PBF, then applied chemical immersion treatment using a FAS-17 ethanol solution to achieve superhydrophobicity. A similar process has also been used by Xing et al. [17] to achieve superhydrophobicity 316L stainless steel by fabricating a cylindrical array structure using L-PBF and chemically treating the surface with an ethanol solution of fluoro-silane. Wang et al. [18] used L-PBF to obtain a mesh structure on ink-printed copper nanoparticles and achieved superhydrophobicity by chemical treatment using fluoro-silane. It is clear that this general approach, adopted by numerous researchers, requires a well-designed surface morphology prior to the chemical treatment, which limits its application to flat surfaces.

Other techniques have also been explored in the literature. Wang et al. [19] also used ink-printed copper nanoparticles via L-PBF to fabricate a superhydrophobic surface by forming nanostructures of amorphous carbon through the decomposition of the polymer PVP. The fabricated surface expressed superhydrophobicity with θ_w as high as 160°. Scanning electrodeposition was used [5] to fabricate superhydrophobic nickel coatings on stainless steel substrates formed by L-PBF. The as-built coatings were hydrophilic immediately following application. However, after one week of air exposure, wettability ranging from superhydrophobic ($\theta_w = 152.3°$) to relatively hydrophobic ($\theta_w = 112.6°$) was observed. Post-processing by laser texturing is another way to alter the surface wettability of L-PBFed parts. Mekhiel et al. [7] textured 316L stainless steel surfaces made by L-PBF to create pillar arrays and channel patterns. Their results showed that the textured surfaces exhibited contact angle values of up to 141°, a significant increase over the range (80°-100°) exhibited by the as-built surfaces. Jiao et al. [9] superimposed femtosecond laser induced period surface structures (LIPSS) onto L-PBFed Ti6Al4V parts. The as-built sample displayed hydrophilic behavior (θ_w~73°), while the surfaces with LIPSS showed a much larger θ_w (90°-150°) after ten days of air exposure.

Surface modification is also not limited to hydrophobicity. Hydrophilicity on L-PBFed alloys can also be achieved. Zhao et al. [20] addressed the effect of electrochemical anodization post-treatment on wettability and as a consequence improved cell adhesion in biomedical applications for L-PBFed Ti6Al4V. They observed that θ_w for L-PBFed Ti6Al4V decreased from 68° to 11° following anodization post-processing, along with an increase in protein absorption and cell adhesion without any distinct effect on the surface roughness. Researchers also used acid etching to modify the surface wettability of TA6V titanium alloy fabricated by L-PBF [10]. Surfaces treated with a 3% HF/10% HNO_3 acid bath showed a significant decrease of θ_w (from 75° to 48°) after the first 15 minutes of etching.

While the aforementioned surface engineering methods successfully modified surface wettability, the fundamental mechanism and coupled effect of surface topography and surface chemistry on the resulting wettability regime are poorly understood for 3D-printed parts. In some studies, the obtained surfaces show unstable wettability, transitioning to superhydrophobicity following extended exposure to air [5,9,17]. Further, much of the current work is focused on lotus leaf superhydrophobicity (high static water contact angle and low contact angle hysteresis/adhesion). The other main category of superhydrophobicity, namely the rose petal effect, where the surface exhibits a high contact angle hysteresis coupled with a high static contact angle, has yet to be investigated. This study explores a more expanded view of superhydrophobicity ranging from low to high surface adhesion by considering both surface topography and chemistry. To the authors' best knowledge, this study constitutes the first attempt at evaluating the rose petal effect for L-PBFed metal alloys.

2. Methods

We have previously developed a nanosecond laser-based high-throughput surface nanostructuring (n-HSN) process [21–24], which simultaneously creates random nanostructures and attains desirable surface chemistry over large-area metallic alloy surfaces. By altering processing conditions, n-HSN treated surfaces can be tuned to display

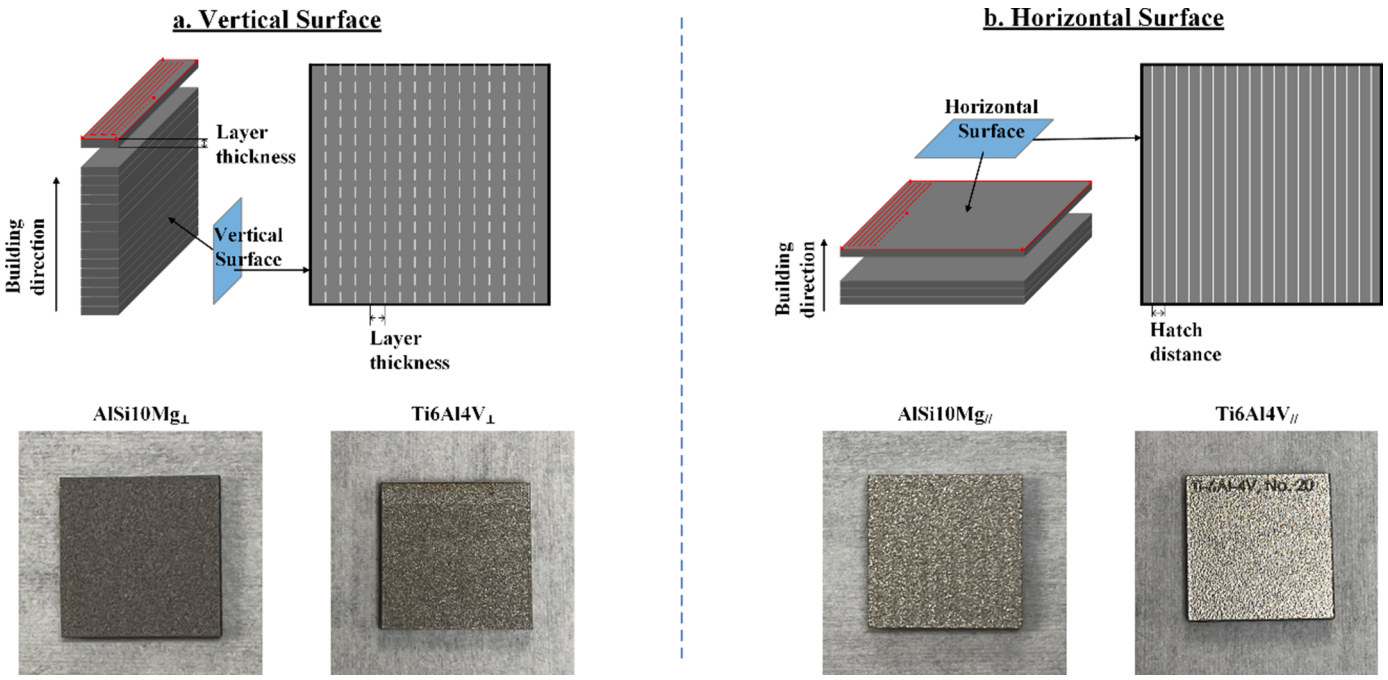

Fig. 2. Design of L-PBF experiments in this study: (a) vertical surface (surface parallel to the building direction) samples (b) horizontal surface (surface parallel to the building platform) samples.

different wetting behaviors ranging from superhydrophobicity to superhydrophilicity. Based on the knowledge gained from n-HSN, two processing methods are proposed in this work for generating superhydrophobicity on metallic surfaces produced by L-PBF.

As illustrated in Fig. 1, method I attempts to chemically functionalize the surfaces without actively modifying the as-built (L-PBF) topography. During the proposed chemical immersion treatment (CIT), the L-PBFed parts are immersed in an ethanol solution of 0.25 wt% chlorosilane reagent [$CF_3(CF_2)_9(CH_2)_2SiCl_3$], also known as FDDTS, for three hours. The surfaces are then cleaned with deionized water, dried with compressed nitrogen, and kept in a vacuum chamber at 80°C for half an hour. Method I will achieve stable surface chemistry for L-PBF parts within a facile, one-step process, whereupon treated surfaces will retain their wetting behavior even following prolonged exposure to air. However, it is noted that the inherently rough surface texture from L-PBF remains unchanged during this CIT-only approach, so the capability of tuning superhydrophobicity via CIT is expected to be limited.

Method II implements the HSN process, simultaneously engineering both surface topography and chemistry. Method II consists of two steps as follows: (1) The part surface is first raster-scanned over the designated region in air using a pulsed laser. Given that 3D printed surfaces have as-built roughness levels in the tens of microns, the effect of laser surface texturing on these already rough surfaces needs to be evaluated. Both nanosecond (n-HSN) and picosecond (p-HSN) lasers are proposed to induce periodic channel patterns on top of 3D printed parts with a channel size on the order of hundreds and tens of microns, respectively. (2) The laser-patterned surface is then subjected to the same CIT as stated in method I. The coupled changes in surface topography and chemistry will induce superhydrophobicity and their contributions will be investigated.

Two representative engineering alloys, AlSi10Mg and Ti6Al4V, are selected in this study for their good weldability [25] and popularity in AM. L-PBF will be used to fabricate the parts for its low cost and good repeatability [26]. Parts for this study are produced by the Quad City Manufacturing Lab using as EOS M270. Two different build orientations are adopted, namely horizontal and vertical, to create different surface topographies as shown in Fig. 2. The horizontal orientation (denoted by the subscript //) means the inclination of the part surface with respect to the build plane is 0°, while the vertical orientation (denoted by the subscript ⊥) indicates the inclination is 90°. Two basic scan strategies were employed on each layer: 1) striping scans and 2) contouring scans (as illustrated in Fig. 2). The bulk of each layer is fused with striping scans. However, the start/stop points of striping scans cause surface irregularities. The vertical test surfaces are comprised of the cross-section of the fused powder layers, so a laser contouring scan is used on the outer edge of each layer to facilitate blending of the irregularities associated with the start/stop points of the laser striping scan. The L-PBF operation parameters, including the continuous wave (CW) fiber, laser are given in Table 1.

In method II, two types of laser source, nanosecond laser (n-HSN) and picosecond laser (p-HSN), were used to create microchannels of various sizes. The high-energy nanosecond pulsed laser with one set of parameters was applied in a single-pass scan for the experiments. Both channel width and depth were in the hundreds of microns due to the high energy intensity per pulse. The high repetition rate picosecond laser was applied in both single-pass and multi-pass scan strategies for

Table 1
L-PBF operational parameters for the aluminum and titanium parts

Surface	CW laser power P (W)	Scan speed V (mm/s)	Powder size d_p (μm)	Hatch distance h (mm)	Layer thickness t (mm)	Energy density E_d $\left(E_d = \frac{P}{Vht}\right)$ (J/mm^3)
AlSi10Mg$_\perp$	150	1250	20-63	0.2	0.03	20
AlSi10Mg$_{//}$	193.6	800	20-63	0.2	0.03	40.3
Ti6Al4V$_\perp$	150	1250	15-45	0.1	0.03	40
Ti6Al4V$_{//}$	170	1250	15-45	0.1	0.03	45.3

Table 2
HSN laser texturing parameters for the L-PBFed parts

Laser	Laser power P (w)	Laser spot diameter d_l (μm)	Scan speed V (mm/s)	Pulse repetition rate R_p (Hz)	Line spacing h (μm)	Laser fluence F $\left(F=\frac{4P\times10^8}{R_p\pi d_l^2}\right)$ (J/cm^2)
Picosecond laser	0.87	15	100	40000	20, 30, 60	12 per pass
Nanosecond laser	0.75	100	0.75	10	300	955

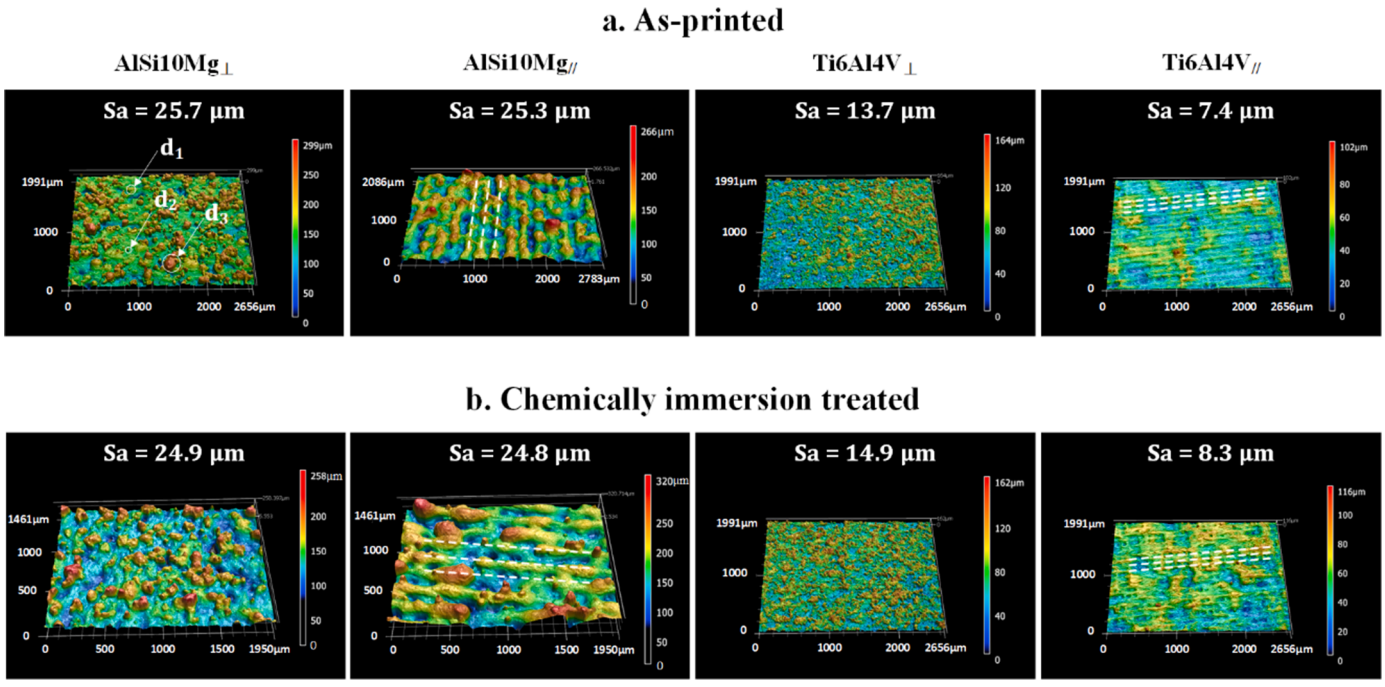

Fig. 3. Surface topography of metal L-PBFed part surfaces: (a) as-printed parts; (b) parts treated by method I: CIT. 3D printing surface defects are noted: d_1 represents balling, d_2 represents partially melted powder, d_3 represents spatter, and white dash lines correspond to laser scan lines used in L-PBF.

the experiments. The corresponding channel width and depth were in the tens of microns, an order of magnitude smaller than the channels created by the nanosecond laser. The effects of channel depth and spacing were also investigated for the picosecond laser. The picosecond and nanosecond laser parameters, selected specifically to generate different surface topographies, are listed in Table 2.

Wetting behaviors of the samples were evaluated by static contact angle measurement and dynamic water droplet run-off experiments. Static contact angles and contact angle hysteresis were measured using a contact angle goniometer (Rame-Hart model 100) coupled with a high-resolution CMOS camera (6–60 × magnification, Thor Laboratories). Dynamic water droplet behavior was characterized by droplet run-off experiments using a low-speed wind tunnel. The surface topography was systemically characterized using a confocal microscope (Keyence VK-X1000). Surface functional groups were analyzed using a Kratos Axis ultrahigh-performance X-ray photoelectron spectroscopy (XPS) system. Surface topography and chemistry were also characterized by a Hitachi S-3400N Scanning Electron Microscopy (SEM) combined with a Bruker Energy-Dispersive Spectroscopy (EDS) system to determine chemical compositional information such as relative abundance and spatial distribution.

3. Results and discussion

3.1. Surface topography

The surface topographic characteristics of the as-built parts were first analyzed using confocal microscopy, as shown in Fig. 3. Though the surface morphology of horizontal surfaces is predominantly governed by surface defects and material properties, the surface morphology of vertical surfaces is predominantly governed by partially fused satellite particles which are directly adjacent to the vertical surface at the vertical surface/powder interface. When the vertical surfaces are fused by the contouring laser scans, the satellite particles remain mostly spherical in shape and are fused to the vertical surface. For horizontal surfaces the factors that contribute to surface defects include laser-induced evaporation of certain elements from the melt pool during L-PBF, material conductivity and the resulting thermal gradients, and partially fused powder particles [27]. Materials containing elements with sufficiently low evaporation temperatures, such as Mg, Zn, and Mn, can exhibit spatter due to melt pool volatility. Large thermal gradients can cause balling, shrinkage/cracking, and the formation of oxide layers. Partially fused powder particles can also play a role in surface topography.

As shown in Fig. 3a, for titanium alloy, the vertical surface (S_a = 13.7 μm) has a larger surface roughness than the horizontal surface (S_a = 7.4 μm). In contrast, aluminum alloys have higher surface roughness values across the board, and the roughness is nearly the same between the horizontal surface (S_a = 25.3 μm) and the vertical surface (S_a = 25.7 μm). This is mainly due to the higher thermal conductivity of the AlSi10Mg powder as excessive heat is transferred away from the melt pool and the formation of oxide layers on top of the melt track causes shrinkage during the L-PBF process [28]. Therefore, the AlSi10Mg surface shows higher surface roughness compared with Ti6Al4V.

The surface topography measurements of the parts processed under

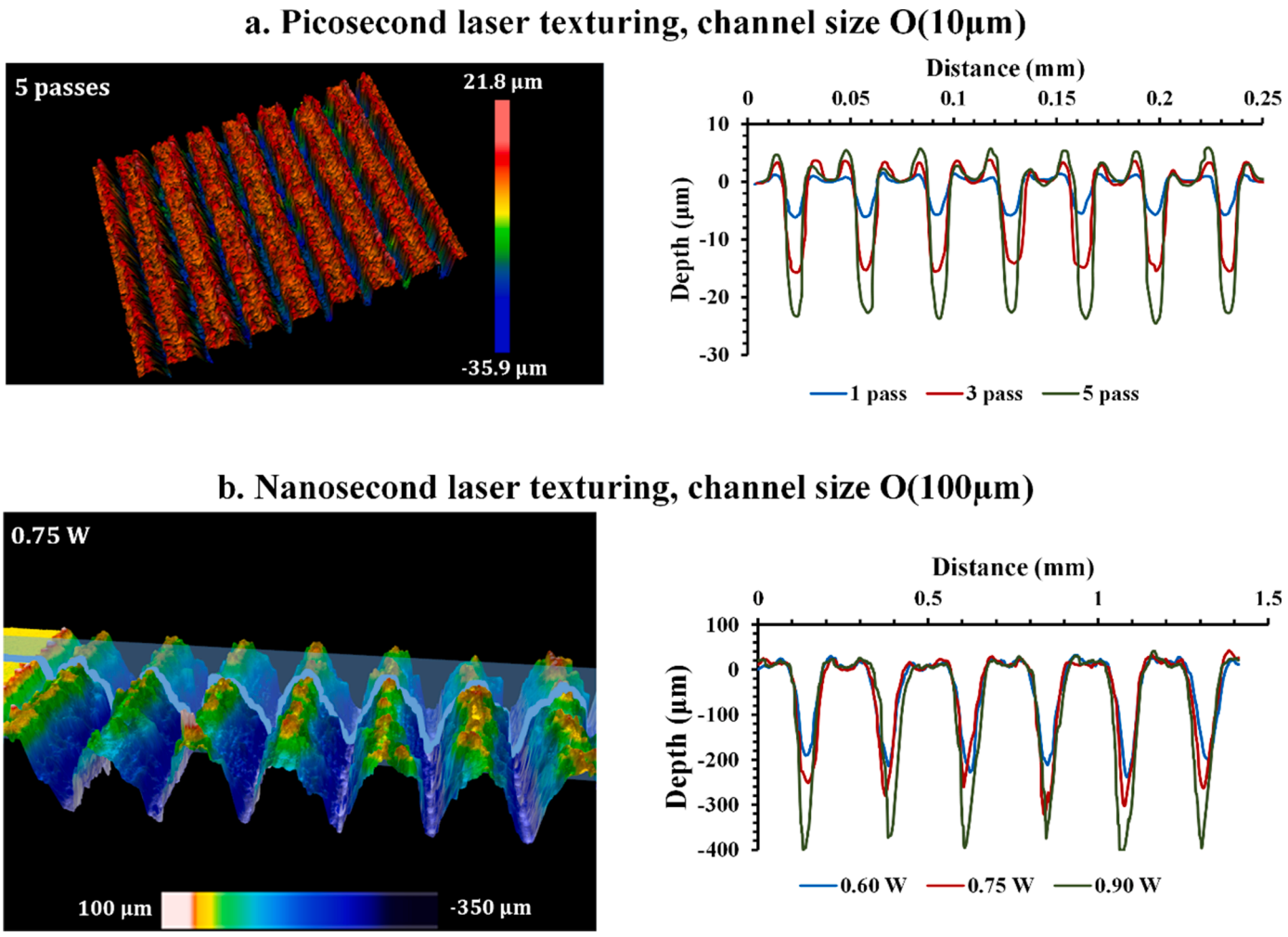

Fig. 4. Laser surface texturing of flat and smooth (polished to a surface roughness less than 0.5 μm) aluminum 6061 alloy plates. (a) Multiple-pass picosecond laser scanning and (b) single-pass nanosecond laser scanning. It is noted that the size of the channels, O(100μm), created by nanosecond laser is one order of magnitude larger than the size of the channels, O(10μm) by the picosecond laser.

CIT in Fig. 3b show that the surface topography does not significantly change after the chemical treatment. The vertical surfaces show more random surface structures, while traces of the laser scanning lines remain on the horizontal surfaces. Surface roughness values similar to those of the as-built parts were obtained, indicating that the chemical etching effect of the FDDTS reagent is minor and does not significantly alter the surface topography.

Since the as-built surfaces have a relatively high surface roughness on the order of tens of microns, it is difficult to accurately determine the channel size resulting from n-HSN and p-HSN texturing of these surfaces. In order to accurately measure the channel geometries and establish the relation between laser processing parameters and channel size, a set of preliminary experiments were performed on a flat metal surface with a surface roughness of under 1 μm. As shown in Fig. 4, the flat aluminum alloy surface clearly showed the microchannels created by picosecond and nanosecond laser treatment. For the picosecond laser, the channel depth is on the order of ten microns, which is within a similar range as the existing surface features from L-PBF. Thus, the picosecond laser will not remove these original surface features. Instead, the microchannels will be superimposed on top of the L-PBFed surface, retaining many of the original asperities. For the nanosecond laser, laser power levels ranging from 0.6 W to 0.9 W corresponded with 200-400 μm channel depths, which is an order of magnitude larger than the original surface features of the L-PBFed parts. Therefore, at all tested power levels, the nanosecond laser will eliminate all original surface features from L-PBF and create new microchannels. In the following study, we selected 0.75 W as a typical nanosecond laser power for all the different L-PBFed parts.

Based on the knowledge gained from the preliminary study, we know that p-HSN will superimpose microchannels on the original surface structures, while n-HSN will fundamentally alter the surface topography of L-PBFed parts to form microchannels. As expected, the picosecond laser textured surfaces partially maintain their original surface topography from the L-PBF process (Fig. 5), with shallow channels present on top of the existing micro-bumps and micro-valleys. The channel depth increases for both AlSi10Mg and Ti6Al4V as the number of laser passes increases from 1 to 5. A denser channel pattern can be obtained when the spacing between the laser scanning lines is reduced, as shown in Fig. 5b. The nanosecond laser processed surfaces, on the other hand, are patterned with microchannels in the hundreds of microns. As shown in Fig. 6, the scanning line traces from the L-PBF process no longer exist on the surface since the laser texturing process in n-HSN removed all original surface features. The same parameters were used on all nanosecond laser processed surfaces, as this method is designed to completely replace the 3D-printed surface texture with micro-channels.

3.2. *Surface wettability*

The θ_w results for the untreated parts (Fig. 7a) show that all the as-built parts are hydrophilic. This is due to the presence of hydroxyl

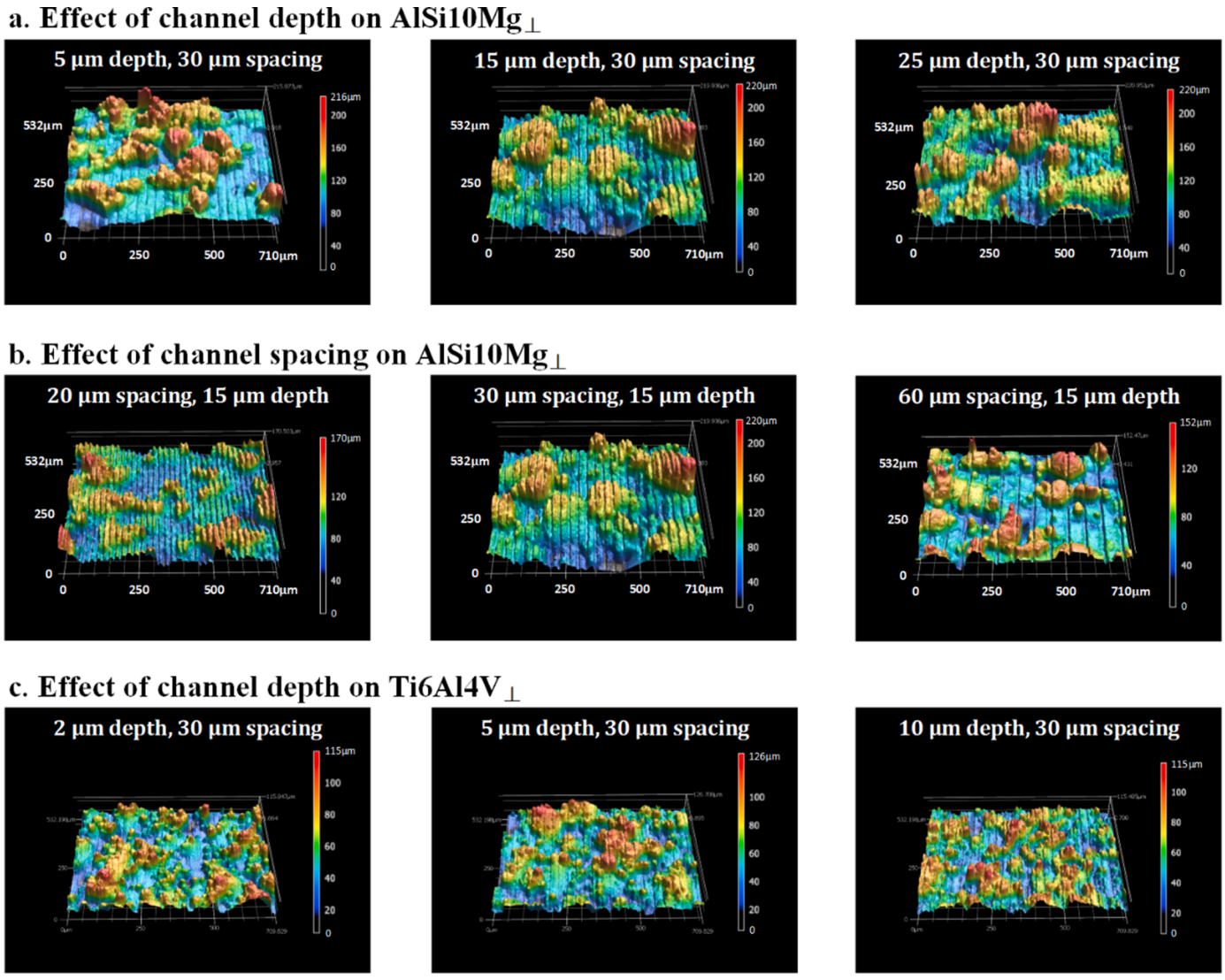

Fig. 5. p-HSN laser textured surface profiles of 3D printed parts. (a) Effect of channel depth for aluminum; (b) channel spacing for aluminum; (c) depth for titanium.

groups on the metal surfaces [29]. After storage in air for one month, an increase of θ_w is observed. The increase of θ_w is due to the reduction of surface energy resulting from the adsorption of organic constituents, including long-chain hydrocarbons with carbonyl groups, carboxylic acids, and diol groups [30,31].

Given that the as-built part surfaces are unstable in terms of wettability, CIT was applied to achieve stable superhydrophobicity (method I). During CIT, the surfaces were functionalized with fluorocarbon groups to reduce the surface energy. Prior study has shown this CIT-induced hydrophobicity to be stable for more than 30 days [32]. The θ_w measurement results for the surfaces under CIT can be found in Fig. 7b. Both AlSi10Mg⊥ and AlSi10Mg$_{//}$ samples achieve superhydrophobicity ($\theta_w > 150°$). The Ti6Al4V samples show only moderate hydrophobicity, with the Ti6Al4V⊥ achieving θ_w~140° and the Ti6Al4V$_{//}$ having θ_w~120°. For AlSi10Mg, the microstructures generated in the L-PBF process, along with the nanostructures resulting from the etching effect of the chlorosilane reagent endow the surface superhydrophobicity. For Ti6Al4V, on the other hand, the relatively smaller surface roughness and scarcity of microstructures created during fabrication led to weaker hydrophobicity. The contact angle hysteresis (θ_H), defined as the difference between the advancing contact angle and the receding contact angle, was measured as well to characterize the surface water adhesion [33]. Samples of all CIT processing conditions display high θ_H ($> 60°$). Even for the superhydrophobic AlSi10Mg surfaces, a high θ_H ($> 90°$) was observed, indicating high droplet-surface adhesion, a classic example of the rose petal effect.

Fig. 8a presents the results of θ_w and θ_H for samples processed by n-HSN (method II). Unlike the CIT-only process (method I), method II achieved superhydrophobicity in all conditions, including on the titanium alloys. Further, θ_H measurements show that the 3D printed metal surfaces processed by n-HSN have low θ_H ($\sim 10°$), indicating that n-HSN can generate lotus leaf superhydrophobicity on L-PBFed metallic parts, with both high static contact angle and low contact angle hysteresis. The wettability of the surfaces treated by p-HSN is shown in Fig. 8b. Similar to n-HSN, all p-HSN treated surfaces achieved the lotus leaf effect, exhibiting θ_w values as high as 160° and θ_H values lower than 10°. For both AlSi10Mg and Ti6Al4V parts, the superhydrophobicity is enhanced when the number of passes increases from one to five. Additionally, the superhydrophobicity of aluminum increases when the laser scan line spacing decreases from 60 µm to 20 µm. These results indicate that the lotus effect can be achieved without completely altering the surface topography—the superimposition of microchannels on the original morphology is sufficient to induce superhydrophobicity. When more and deeper channels are present, the surface superhydrophobicity is further improved.

The water droplet run-off behavior of the AlSi10Mg⊥ surfaces was

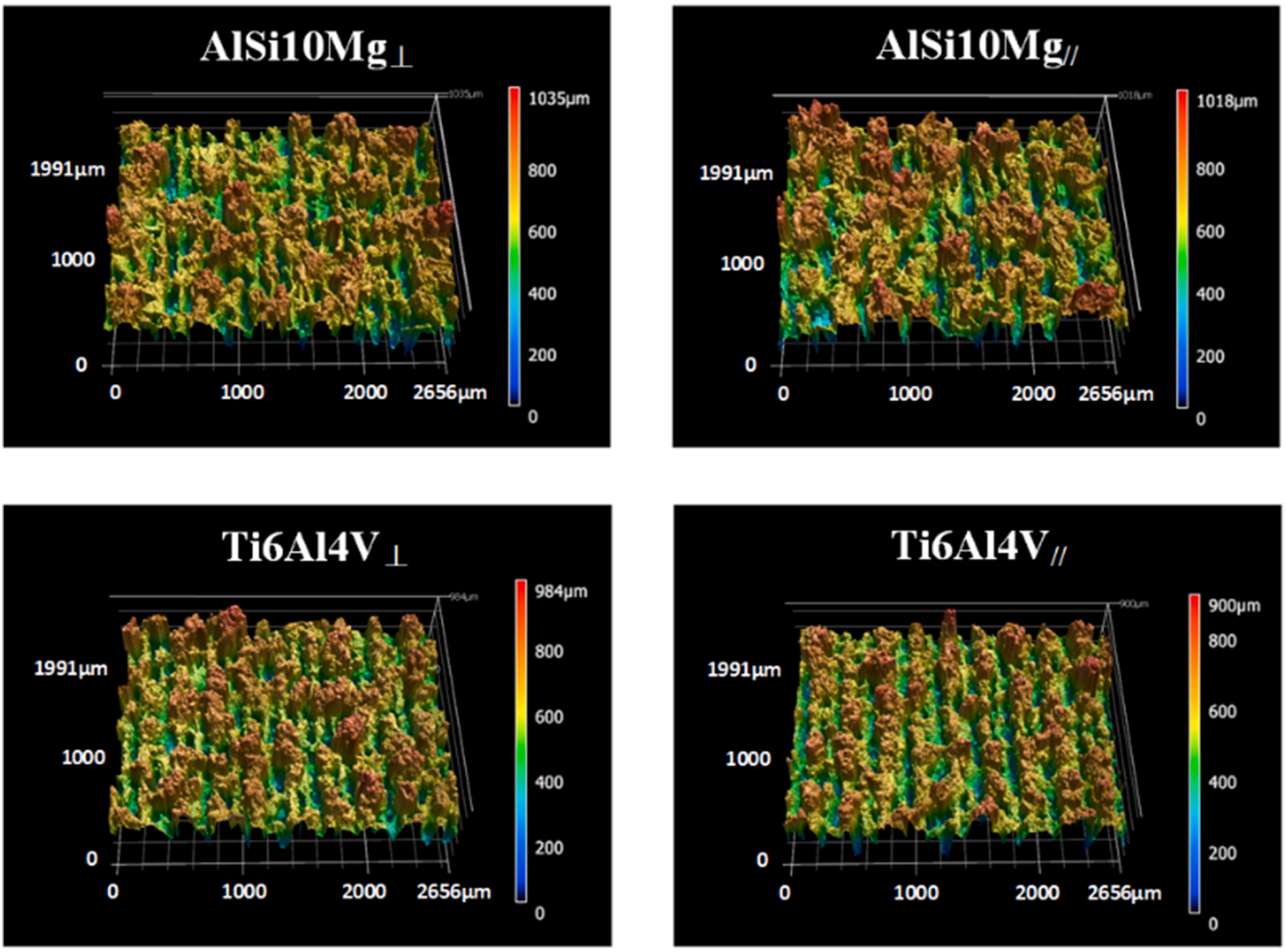

Fig. 6. Surface topography of the L-PBFed parts processed by n-HSN, showing that the surface features were completely replaced by the microchannels created by the nanosecond laser.

studied by wind-driven droplet run-off experiments. Fig. 9a shows a schematic of the experimental setup used to quantify the dynamic run-off process for wind-driven water droplets over the test surface. Droplet displacement in relation to the freestream velocity measurements are shown in Fig. 9b. The results indicate drastically different behavior for surfaces treated by CIT only and n-HSN. For the CIT-only surface, the droplet fails to roll off even when exposed to wind velocities greater than 10 m/s. Instead, the droplet is elongated to about one millimeter along the freestream direction. In stark contrast, for the n-HSN surface, the droplet easily runs off the surface at a wind velocity of just 4 m/s, with negligible droplet elongation. The droplet displacement results correspond to the θ_H results, denoting the rose petal effect for the CIT-only surface and the lotus leaf effect for the n-HSN surface.

3.3. Role of surface chemistry

To determine the functional groups present on the treated surfaces, XPS analysis was performed on a chemically treated flat aluminum alloy surface. As illustrated in Fig. 10, -CF_3 and -CF_2- functional groups were detected in the F1s signal, which originates from the FDDTS reagent used in CIT. These fluorocarbon functional groups help reduce the surface energy and therefore increase the surface hydrophobicity.

In order to quantitatively measure the surface functional groups, the surface elemental composition of L-PBFed AlSi10Mg was further examined using EDS analysis. Elements including Al, Si, Mg, F, O, and C were all detected on these surfaces. The EDS mappings of fluorine as the main element in the superhydrophobic functional groups were collected from surfaces treated by CIT, p-HSN, and n-HSN, respectively. For the CIT treated samples, the fluorine species distribute randomly over the surface, indicating fluorocarbon functional group (-CF_2- and -CF_3) adsorption over the entire surface. The fluorine content measurements (Fig. 11) show that even though the same chemical treatment process is applied to the CIT-only surface and HSN surface, the fluorine concentration is not the same for these surfaces. The surfaces treated by n/p-HSN contain four times more fluorine than the surface treated by CIT alone. This enormous difference in fluorine content is due to the enhanced chemical reaction between FDDTS chemical species and the laser textured surface. Laser texturing induces surface oxidation and hydroxylation [34], effectively boosting the chemical reaction between FDDTS and surface oxides. The metal oxides and hydroxyl groups serve as the potential sites for this chemical reaction, allowing the fluorocarbon chains to more easily anchor to the top of the surface [35]. The difference in surface chemistry contributes to the formation of different wetting regimes. The surface treated by CIT only does not contain enough fluorine to sufficiently reduce water adhesion, resulting in the rose petal effect, while the abundance of fluorine on n/p-HSN surfaces enhances hydrophobicity, leading to the low-adhesion lotus effect.

For the HSN treated samples, the surface chemistry distribution is inhomogeneous due to the laser-patterned surface topography, as shown in Fig. 11. The fluorine species are only detected on the peaks between

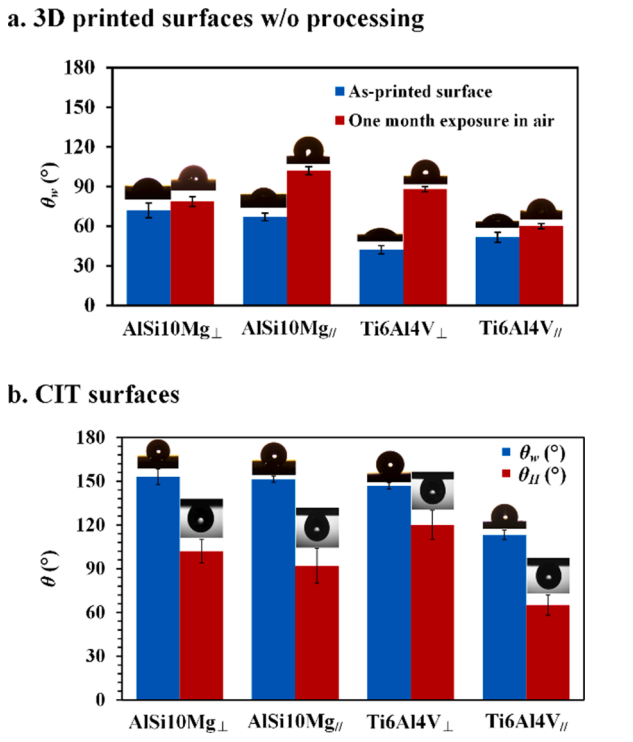

Fig. 7. (a) Surface wettability of as-printed metal parts. Water contact angles increase after one month storage in air indicating unstable surface wetting for these metal 3D printed surfaces; (b) Rose petal superhydrophobic parts treated by CIT.

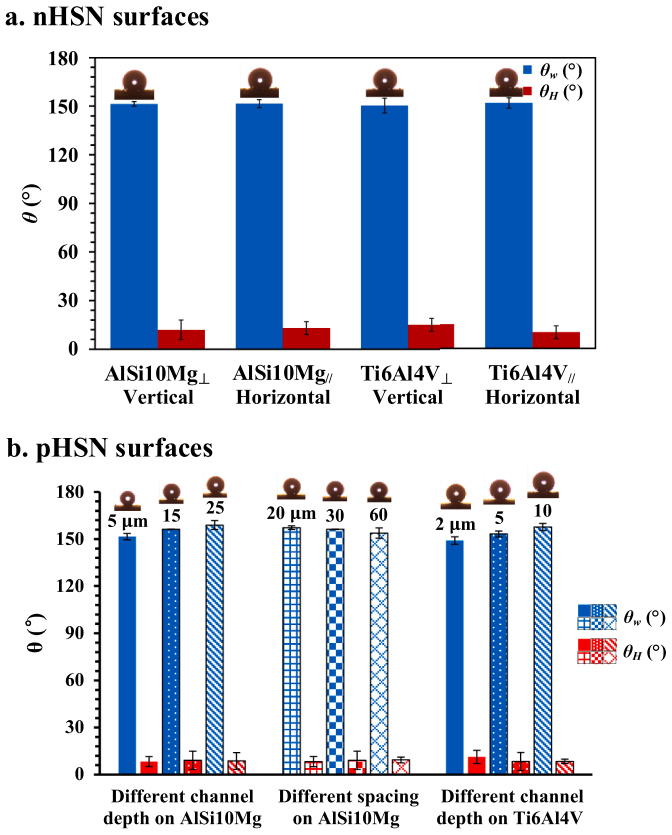

Fig. 8. Lotus leaf superhydrophobic surfaces processed by (a) n-HSN and (b) p-HSN.

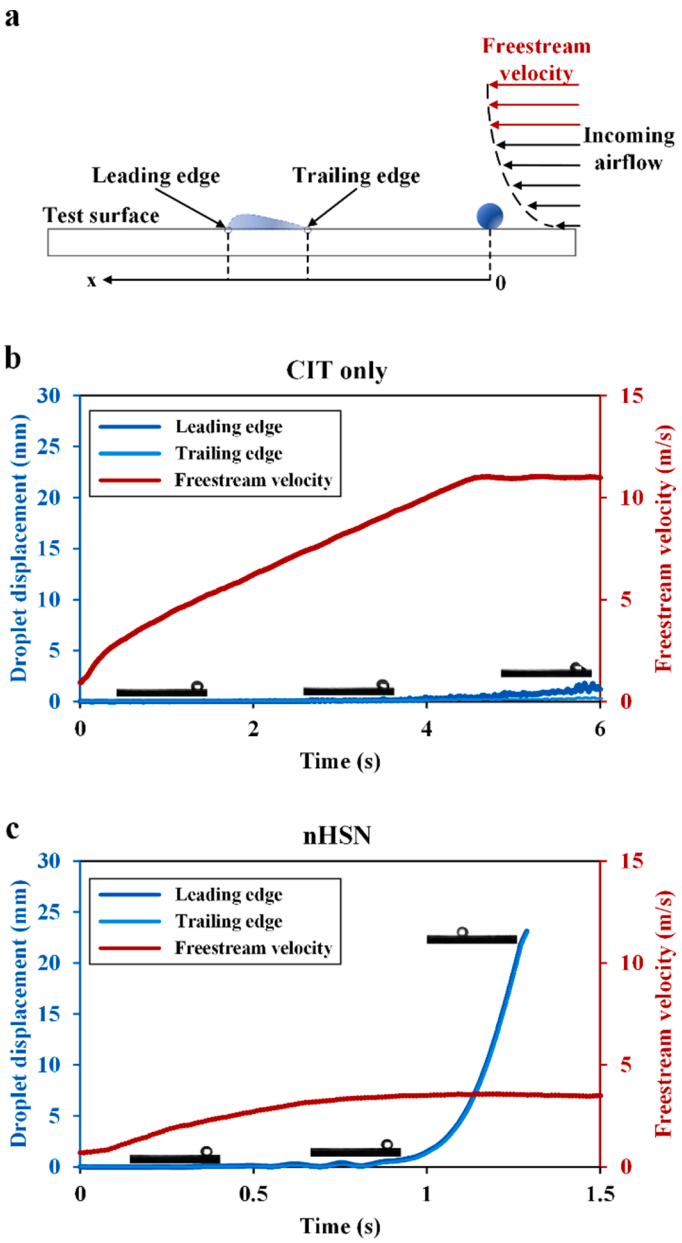

Fig. 9. Analysis of dynamic droplet adhesion behaviors. (a) Wind-driven droplet run-off experiments. (b) Droplet displacement and freestream velocity of surfaces treated by CIT only, demonstrating the high-water adhesion. (b) Droplet displacement and freestream velocity of surfaces treated by n-HSN, showing the low water adhesion.

adjacent channels. This, however, does not mean that fluorine is not present inside the channels. The micro-asperities left behind from L-PBF-induced roughness can interfere with electron beams, causing any fluorine content in the micro valleys to go undetected by the EDS analysis. In other words, the surface features around the peaks will block part of the signal from the troughs, as the feature size of the textured surface is much larger than the wavelength of the incident and outgoing radiation for EDS. Therefore, the electron beam is unable to penetrate into the deeper areas (micro-valleys) [36]. Meanwhile, the channel depth is on the order of hundreds of microns for nanosecond laser treatment and tens of microns for the picosecond laser, which is many orders of magnitude larger than the X-ray penetration depth [37–39]. Hence the emitted X-rays are reabsorbed by the substrate before they can make it to the EDS detector, which makes the fluorine content in the channels undetectable. Despite this fundamental limitation of EDS as a

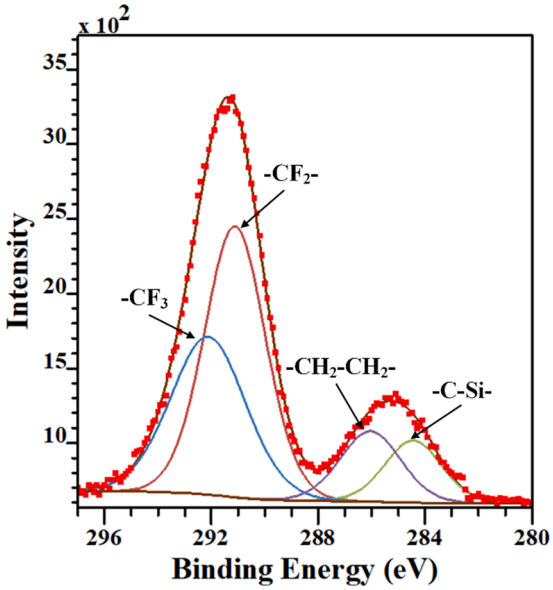

Fig. 10. Surface chemical functionalization characterized using core-level XPS analysis of C 1s at the aluminum alloy surface, showing the existence of -CF_2-, -CF_3 superhydrophobic functional groups.

surface chemistry analysis technique, EDS is still considered a powerful semi-quantitative technique to investigate surface chemical composition [40].

3.4. Role of surface texture

Surface wettability is determined by the coupled effect of surface chemistry and surface topography [41]. To characterize the rose petal and lotus effects, two main wetting regimes have been widely used over the past few decades, i.e., Wenzel [42] and Cassie-Baxter [43]. In the Wenzel regime, water droplets penetrate the surface asperities and fully wet the surface, consequently displaying greater water adhesion. The apparent contact angle (θ_W) was proposed as:

$$\cos(\theta_W) = r\frac{\gamma_{sv} - \gamma_{sl}}{\gamma_{lv}} \quad (1)$$

where r is the solid surface roughness ratio, which represents the ratio of solid surface area to the projected area, and γ is the intrinsic surface energy per unit area, which is influenced by the surface chemistry. The subscripts *sv, lv*, and *sl* stand for solid-vapor, liquid-vapor, and solid-liquid interfaces, respectively. In the Cassie-Baxter regime, gas is entrapped between the liquid and solid surface within the troughs of the surface roughness, preventing complete surface wetting and leading to lower water adhesion. In this regime, only a fraction f ($0 < f < 1$) of r contributes toward the solid-liquid interface. The apparent contact angle (θ_{CB}) is then given by [44]:

$$\cos(\theta_{CB}) = rf\frac{\gamma_{sv} - \gamma_{sl}}{\gamma_{lv}} + f - 1. \quad (2)$$

Both of these regimes only account for surface tension and do not consider the various components and inhomogeneous distribution of surface chemistry that influence the interfacial surface tension. Therefore, it is difficult to apply the above equations to real-world surfaces, particularly L-PBFed surfaces, which feature complex surface topographies and inhomogeneous surface chemistry. Moreover, both of the models use r as the only parameter to describe the surface morphology, accounting only for the magnitude of surface roughness. Information on the complex shape and curvature of surface topographies is lost when only using this single parameter.

In our study, we employ an additional parameter, S_{pc}, to capture the shape of the surface and to quantitatively characterize the surface topography difference between the CIT-only and n/p-HSN surfaces. S_{pc} is the arithmetic mean peak curvature of the surface, which is expressed by the equation:

$$S_{pc} = -\frac{1}{2}\frac{1}{n}\sum_{k=1}^{n}\left(\frac{\partial^2 z(x,y)}{\partial x^2} + \frac{\partial^2 z(x,y)}{\partial y^2}\right) \quad (3)$$

where $z(x,y)$ stands for the height measured from the average surface plane, and n is the number of peaks in the concerned area [45]. Larger values of S_{pc} correspond to sharper points of contact (peaks), while lower values indicate more rounded peaks. In this study, the S_{pc} parameter is used to characterize the surface structure only at a microscale level, as wetting of the microstructure is sufficient to enter the rose petal regime, irrespective of the penetration (or lack thereof) of the nanostructure [46].

The r and S_{pc} values of the AlSi10Mg and Ti6Al4V surfaces under various processing conditions are shown in Fig. 12. It can be clearly seen that all n-HSN processed samples show relatively larger S_{pc} values (> 4/

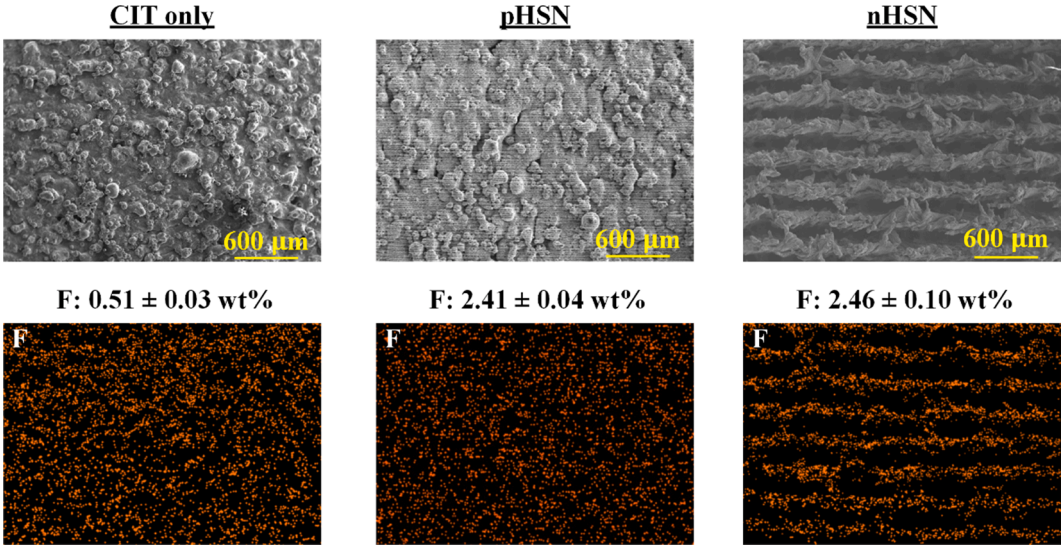

Fig. 11. Fluorine distribution on AlSi10Mg surfaces treated by CIT only, p-HSN and n-HSN, respectively. The orange spots in the images at the bottom row represent the fluorine species on the surfaces.

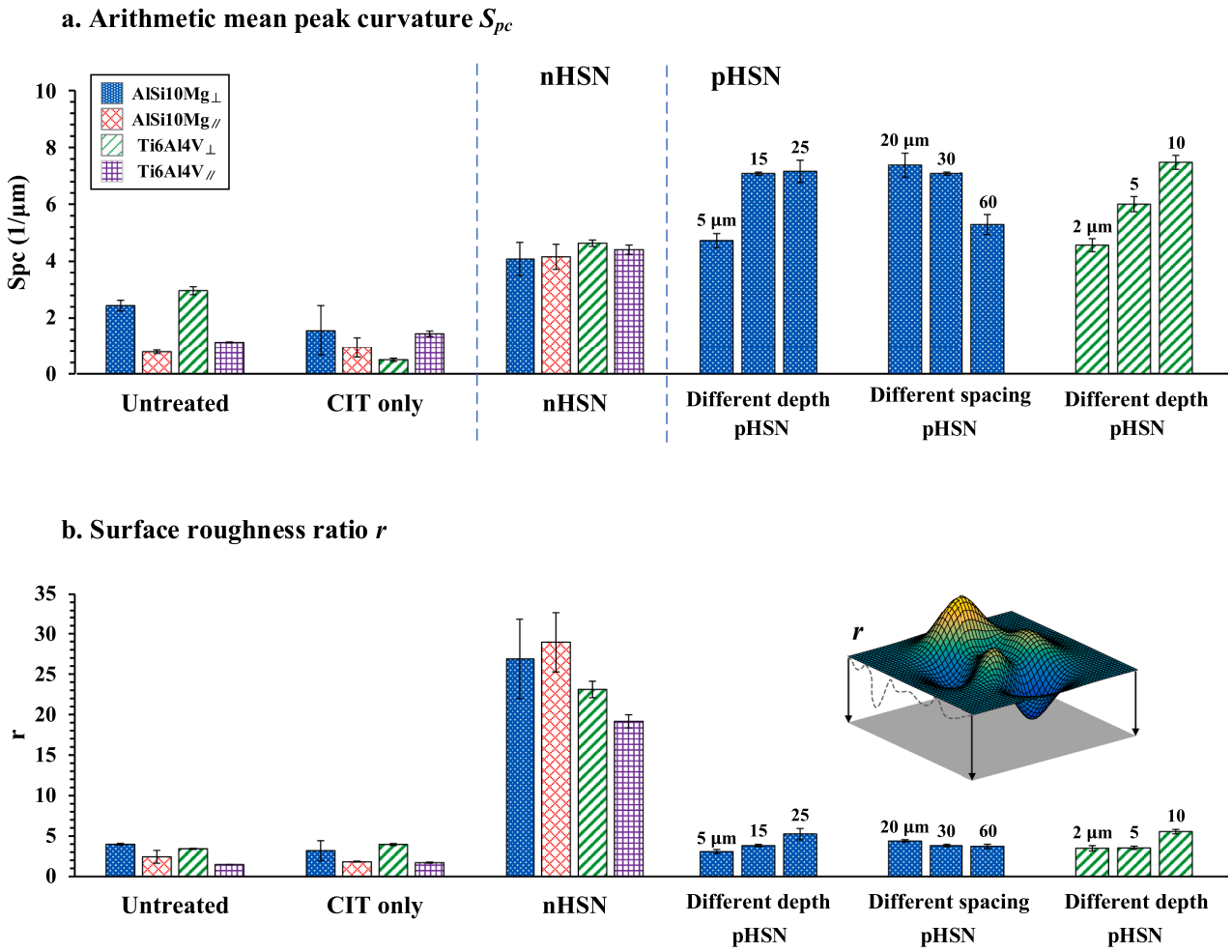

Fig. 12. Effects of surface texture: (a) S_{pc} values of parts under various treatment conditions. (b) r values of parts under various treatment conditions.

μm), indicating that the surface features are pointier in nature. The surfaces processed by the picosecond laser have even higher S_{pc} values than the nanosecond laser textured surfaces due to the higher energy concentration and smaller laser spot size of the former. As the number of laser passes increases, the S_{pc} values also increase, indicating that the microchannels become sharper and deeper. When the spacing between laser scan lines increases, the density of the channels is reduced, and the S_{pc} values decrease accordingly. The untreated and CIT-only surfaces have more rounded features and less fluctuation, leading to small S_{pc} (~ 2/μm) and r (< 4) values. Worth noting, however, is that the r value is not necessarily large for the HSN surfaces. The surfaces processed by n-HSN have large r values (> 15) as the surfaces show high fluctuation due to the deep channels created by the nanosecond laser, but the surfaces processed by p-HSN show similar r values as the untreated and CIT surfaces. This is because the original surface topography was not fully removed during p-HSN treatment, as shown in Fig. 5, and only a mild change in surface morphology was induced by the picosecond laser. Given that both n-HSN and p-HSN achieved lotus leaf super-hydrophobicity with drastically differing r values, it is clear that S_{pc} is a more effective predictor of wetting regime than simply using the roughness ratio r. When deep and pointed microstructures are present, large S_{pc} values are obtained, and the surface is subject to the Cassie-Baxter state. Air is entrapped inside the valleys, reducing the contact area between droplets and surface features, leading to low water adhesion (lotus effect). When the surface structures are flatter, the water completely wets the valleys in the Wenzel state, increasing contact area and adhesion (rose petal effect) [47].

4. Conclusions

This work presented two novel surface wettability modification methods, CIT and HSN, capable of tuning the surface topography and chemistry for metal parts fabricated by L-PBF. The research concludes the following:

1 A wettability transition towards hydrophobicity was observed for L-PBFed metal parts after exposure to air for over a month. While as-built parts are hydrophilic immediately following fabrication, an increase of 5°-45° in θ_w was observed after one month of air exposure. The adsorption of organic molecules in air is responsible for this phenomenon.
2 Superhydrophobic lotus leaf surfaces exhibiting low water adhesion were achieved for both aluminum and titanium printed alloy parts by modifying surface chemistry and topography through HSN post-processing. Superhydrophobic rose petal wetting with high water adhesion was achieved on metal printed parts by standalone CIT. These resulting surface wettabilities are stable in air.
3 Surface chemistry, both qualitative (species present) and quantitative (surface coverage) determines water adhesion levels. More fluorocarbon functional groups are present on the surface treated by HSN than on the surface only treated by CIT, resulting in lower water adhesion for the former. This is due to the enhancement of surface oxidation during the laser texturing step in HSN. The fluorine species lower the surface energy and reduce water adhesion.
4 Surface texture also plays an important role in surface wetting behavior. S_{pc} is a more useful parameter than r in the

characterization of surface topography for lotus leaf and rose petal wetting regimes. The lotus surfaces displayed larger S_{pc} values ($> 4/\mu m$), indicating the presence of sharp surface microstructures, while the rose petal surface had smaller S_{pc} ($\sim 2/\mu m$) and r (< 4) values, representing a surface with low feature curvature.

Author Contributions

W. Huang conducted the HSN experiments and surface characterizations. B. Nelson prepared for the 3D printed samples. S. Tian and A. Samanta helped with the experimental analysis. R. Ordikhani-Seyedlar and S. K. Shaw contributed to the chemical analysis aspects of the investigation. R.C.Y. Auyeung helped with the picosecond laser processing. C. Lamuta helped with the surface topography analysis. H. Hu helped with the surface characterization. H. Ding developed the theoretical concepts, experimental approach, and supervised the investigation. W. Huang composed the manuscript. H. Ding revised and finalized the manuscript. All participants discussed the results and commented on the manuscript.

Declaration of Competing Interest

The authors declare that they have no known competing financial interests or personal relationships that could have appeared to influence the work reported in this paper.

Data Availability

Data will be made available on request.

Acknowledgement

The authors gratefully acknowledge the financial support by the National Science Foundation under Grant Number CMMI-1762353.

References

[1] D.P. Vega, A.P. Valerga, F.A.O. Orellana, M. Batista, Application of Computer Aided Design and Additive Manufacturing to the recovery of the Paddle Boat by Francesco Di Giorgio, Procedia Manuf. 41 (2019) 1119–1126.
[2] M.A. Arie, A.H. Shooshtari, M.M. Ohadi, Experimental characterization of an additively manufactured heat exchanger for dry cooling of power plants, Appl. Therm. Eng. 129 (2018) 187–198.
[3] C.C. Ho, K. Murata, D.A. Steingart, J.W. Evans, P.K. Wright, A super ink jet printed zinc–silver 3D microbattery, J. Micromechanics Microengineering. 19 (2009) 94013.
[4] J. Sun, W. Wang, Z. Liu, B. Li, K. Xing, Z. Yang, Study on selective laser melting 316L stainless steel parts with superhydrophobic surface, Appl. Surf. Sci. 533 (2020), https://doi.org/10.1016/j.apsusc.2020.147445.
[5] Z. Wang, L. Shen, W. Jiang, M. Fan, D. Liu, J. Zhao, Superhydrophobic nickel coatings fabricated by scanning electrodeposition on stainless steel formed by selective laser melting, Surf. Coatings Technol. 377 (2019), 124886, https://doi.org/10.1016/j.surfcoat.2019.08.015.
[6] J. Neukäufer, B. Seyfang, T. Grützner, Investigation of contact angles and surface morphology of 3D-printed materials, Ind. Eng. Chem. Res. 59 (2020) 6761–6766, https://doi.org/10.1021/acs.iecr.0c00430.
[7] S. Mekhiel, P. Koshy, M.A. Elbestawi, Additive texturing of metallic surfaces for wetting control, Addit. Manuf. 37 (2021), 101631, https://doi.org/10.1016/j.addma.2020.101631.
[8] J. Zhou, X. Han, H. Li, S. Liu, J. Yi, Investigation of layer-by-layer laser remelting to improve surface quality, microstructure, and mechanical properties of laser powder bed fused AlSi10Mg alloy, Mater. Des. 210 (2021), 110092.
[9] L. Jiao, Z.Y. Chua, S.K. Moon, J. Song, G. Bi, H. Zheng, Femtosecond laser produced hydrophobic hierarchical structures on additive manufacturing parts, Nanomaterials 8 (2018), https://doi.org/10.3390/nano8080601.
[10] T. Thenard, A. Catapano, R. Allena, M. El May, N. Saintier, M. Mesnard, Topography and wettability characterization of surfaces manufactured by SLM and treated by chemical etching, Mech. Adv. Mater. Struct. (2020) 1–18.
[11] J. Vaithilingam, S. Kilsby, R.D. Goodridge, S.D.R. Christie, S. Edmondson, R.J. M. Hague, Functionalisation of Ti6Al4V components fabricated using selective laser melting with a bioactive compound, Mater. Sci. Eng. C. 46 (2015) 52–61.
[12] J. Long, M. Zhong, H. Zhang, P. Fan, Superhydrophilicity to superhydrophobicity transition of picosecond laser microstructured aluminum in ambient air, J. Colloid Interface Sci. 441 (2015) 1–9, https://doi.org/10.1016/j.jcis.2014.11.015.
[13] P. Bizi-Bandoki, S. Valette, E. Audouard, S. Benayoun, Time dependency of the hydrophilicity and hydrophobicity of metallic alloys subjected to femtosecond laser irradiations, Appl. Surf. Sci. 273 (2013) 399–407, https://doi.org/10.1016/j.apsusc.2013.02.054.
[14] E. Maleki, S. Bagherifard, M. Bandini, M. Guagliano, Surface post-treatments for metal additive manufacturing: progress, challenges, and opportunities, Addit. Manuf. 37 (2021), 101619, https://doi.org/10.1016/j.addma.2020.101619.
[15] E. Maleki, S. Bagherifard, O. Unal, F. Sabouri, M. Bandini, M. Guagliano, Effects of different mechanical and chemical surface post-treatments on mechanical and surface properties of as-built laser powder bed fusion AlSi10Mg, Surf. Coatings Technol. 439 (2022), 128391, https://doi.org/10.1016/j.surfcoat.2022.128391.
[16] E. Maleki, S. Bagherifard, F. Sabouri, M. Bandini, M. Guagliano, Hybrid thermal, mechanical and chemical surface post-treatments for improved fatigue behavior of laser powder bed fusion AlSi10Mg notched samples, Surf. Coatings Technol. 430 (2022), 127962, https://doi.org/10.1016/j.surfcoat.2021.127962.
[17] L. Xing, J. Yu, Z. Ji, X. Huang, C. Dai, Q. Zhang, Study on preparation of superhydrophobic surface by selective laser melting and corrosion resistance, Appl. Sci. 11 (2021) 7476, https://doi.org/10.3390/app11167476.
[18] X. Wang, J. Liu, Y. He, Y. Wang, Selective laser melting of ink-printed (SLM-IP) copper (Cu) nanoparticles (NPs) for facile controllable fabrication of superhydrophobic surface, Surf. Coatings Technol. 347 (2018) 84–91, https://doi.org/10.1016/j.surfcoat.2018.04.080.
[19] X. Wang, J. Liu, L. Yang, Y. He, Y. Wang, Nano-sized amorphous carbon covered surface formed by selective laser melting of ink-printed (SLM-IP) copper (Cu) nanoparticles (NPs), Appl. Surf. Sci. 448 (2018) 133–137, https://doi.org/10.1016/j.apsusc.2018.04.109.
[20] D.-P. Zhao, J.-C. Tang, H.-M. Nie, Y. Zhang, Y.-K. Chen, X. Zhang, H.-X. Li, M. Yan, Macro-micron-nano-featured surface topography of Ti-6Al-4V alloy for biomedical applications, Rare Met. 37 (2018) 1055–1063.
[21] Q. Wang, A. Samanta, S.K. Shaw, H. Hu, H. Ding, Nanosecond laser-based high-throughput surface nanostructuring (nHSN), Appl. Surf. Sci. 507 (2020), 145136, https://doi.org/10.1016/j.apsusc.2004.11.001.
[22] H. Ding, Q. Wang, A. Samanta, N. Shen, Nanosecond laser-based high-throughput surface nano-structuring (nHSN) process, US20190054571A1, 2019.
[23] A. Samanta, Q. Wang, S.K. Shaw, H. Ding, Nanostructuring of laser textured surface to achieve superhydrophobicity on engineering metal surface, J. Laser Appl. 31 (2019), 022515, https://doi.org/10.2351/1.5096148.
[24] A. Samanta, Q. Wang, G. Singh, S.K. Shaw, F. Toor, A. Ratner, H. Ding, Nanosecond pulsed laser processing turns engineering metal alloys antireflective and superwicking, J. Manuf. Process. 54 (2020) 28–37, https://doi.org/10.1016/j.jmapro.2020.02.029.
[25] D. Dai, D. Gu, M. Xia, C. Ma, H. Chen, T. Zhao, C. Hong, A. Gasser, R. Poprawe, Melt spreading behavior, microstructure evolution and wear resistance of selective laser melting additive manufactured AlN/AlSi10Mg nanocomposite, Surf. Coatings Technol. 349 (2018) 279–288.
[26] E.O. Olakanmi, R.F. Cochrane, K.W. Dalgarno, A review on selective laser sintering/melting (SLS/SLM) of aluminium alloy powders: processing, microstructure, and properties, Prog. Mater. Sci. 74 (2015) 401–477.
[27] M.H. Nasab, D. Gastaldi, N.F. Lecis, M. Vedani, On morphological surface features of the parts printed by selective laser melting (SLM), Addit. Manuf. 24 (2018) 373–377, https://doi.org/10.1016/j.addma.2018.10.011.
[28] Z.Y. Chua, S.K. Moon, Geometric influence of the laser-based powder bed fusion process in Ti6AL4V and AlSi10Mg, (2021) 3165–3176.
[29] J. Long, M. Zhong, H. Zhang, P. Fan, Superhydrophilicity to superhydrophobicity transition of picosecond laser microstructured aluminum in ambient air, J. Colloid Interface Sci. 441 (2015) 1–9, https://doi.org/10.1016/j.jcis.2014.11.015.
[30] A.M. Kietzig, S.G. Hatzikiriakos, P. Englezos, Patterned superhydrophobic metallic surfaces, Langmuir 25 (2009) 4821–4827, https://doi.org/10.1021/la8037582.
[31] R. Jagdheesh, M. Diaz, J.L. Ocaña, Bio inspired self-cleaning ultrahydrophobic aluminium surface by laser processing, RSC Adv. 6 (2016) 72933–72941, https://doi.org/10.1039/C6RA12236A.
[32] A. Samanta, W. Huang, H. Chaudhry, Q. Wang, S.K. Shaw, H. Ding, Design of chemical surface treatment for laser-textured metal alloys to achieve extreme wetting behavior, ACS Appl. Mater. Interfaces 12 (2020) 18032–18045, https://doi.org/10.1021/acsami.9b21438.
[33] D.L. Schmidt, R.F. Brady, K. Lam, D.C. Schmidt, M.K. Chaudhury, Contact angle hysteresis, adhesion, and marine biofouling, Langmuir 20 (2004) 2830–2836.
[34] P. Gregorčič, B. Šetina-Batič, M. Hočevar, Controlling the stainless steel surface wettability by nanosecond direct laser texturing at high fluences, Appl. Phys. A Mater. Sci. Process. 123 (2017) 1–8, https://doi.org/10.1007/s00339-017-1392-5.
[35] A. Samanta, W. Huang, M. Bell, S.K. Shaw, N. Charipar, H. Ding, Large-area surface wettability patterning of metal alloys via a maskless laser-assisted functionalization method, Appl. Surf. Sci. 568 (2021), 150788, https://doi.org/10.1016/J.APSUSC.2021.150788.
[36] W. Huang, R. Ordikhani-Seyedlar, A. Samanta, S. Shaw, H. Ding, Quantification of superhydrophobic functionalization for laser textured metal surfaces, Colloids Surfaces A Physicochem. Eng. Asp. 636 (2022), 128126, https://doi.org/10.1016/j.colsurfa.2021.128126.
[37] C.J. Powell, A. Jablonski, Progress in quantitative surface analysis by X-ray photoelectron spectroscopy: current status and perspectives, J. Electron Spectros. Relat. Phenomena. 178 (2010) 331–346.

[38] C.T. Williams, SJB Reed Electron Microprobe Analysis, 57, Cambridge University Press, Cambridge, 1993, pp. 558–559, 1993. xviii+ 326 pp. Price£ 45.00 (hardback)., Mineral. Mag.
[39] E. Umbach, Practical surface analysis: Auger and X-ray Photoelectron Spectroscopy, (Practical Surface Analysis, Vol. 1), edited by D. Briggs and MP Seah, Wiley, Chichester, 1991,£ 85.00, ISBN 0-471-920819, (1992).
[40] S. Nasrazadani, S. Hassani, Chapter 2 - Modern analytical techniques in failure analysis of aerospace, chemical, and oil and gas industries, in: A.S.H. Makhlouf, M. B.T.-H. of M.F.A. with C.S. from the O. and G.I. Aliofkhazraei (Eds.), Butterworth-Heinemann, 2016: pp. 39–54. 10.1016/B978-0-08-100117-2.00010-8.
[41] W. Huang, A. Samanta, Y. Chen, S. Baek, S.K. Shaw, H. Ding, Machine learning model for understanding laser superhydrophobic surface functionalization, J. Manuf. Process. 69 (2021) 491–502, https://doi.org/10.1016/J.JMAPRO.2021.08.007.
[42] R.N. Wenzel, Resistance of solid surfaces to wetting by water, Ind. Eng. Chem. 28 (1936) 988–994.
[43] A.B.D. Cassie, S. Baxter, Wettability of porous surfaces, Trans. Faraday Soc. 40 (1944) 546–551, https://doi.org/10.1039/TF9444000546.
[44] A. Marmur, Wetting on hydrophobic rough surfaces: to be heterogeneous or not to be? Langmuir 19 (2003) 8343.
[45] L. Hu, D. Yun, J. Gao, C. Tang, Monitoring and optimizing the surface roughness of high friction exposed aggregate cement concrete in exposure process, Constr. Build. Mater. 230 (2020), 117005.
[46] B. Bhushan, M. Nosonovsky, The rose petal effect and the modes of superhydrophobicity, Philos. Trans. R. Soc. A Math. Phys. Eng. Sci. 368 (2010) 4713–4728, https://doi.org/10.1098/rsta.2010.0203.
[47] J. Long, P. Fan, D. Gong, D. Jiang, H. Zhang, L. Li, M. Zhong, Superhydrophobic surfaces fabricated by femtosecond laser with tunable water adhesion: from lotus leaf to rose petal, ACS Appl. Mater. Interfaces. 7 (2015) 9858–9865, https://doi.org/10.1021/acsami.5b01870.